EPJ manuscript No.
(will be inserted by the editor)

Vortex rings and solitary waves in trapped Bose-Einstein condensates

Stavros Komineas[a]

Max-Planck Institute for the Physics of Complex Systems, Nöthnitzer Str. 38, 01187 Dresden, Germany

Abstract. We discuss nonlinear excitations in an atomic Bose-Einstein condensate which is trapped in a harmonic potential. We focus on axially symmetric solitary waves propagating along a cylindrical condensate. A quasi one-dimensional dark soliton is the only nonlinear mode for a condensate with weak interactions. For sufficiently strong interactions of experimental interest solitary waves are hybrids of one-dimensional dark solitons and three-dimensional vortex rings. The energy-momentum dispersion of these solitary waves exhibits characteristics similar to a mode proposed sometime ago by Lieb in a strictly 1D model, as well as some rotonlike features. We subsequently discuss interactions between solitary waves. Head-on collisions between dark solitons are elastic. Slow vortex rings collide elastically but faster ones form intermediate structures during collisions before they lose energy to the background fluid. Solitary waves and their interactions have been observed in experiments. However, some of their intriguing features still remain to be experimentally identified.

1 Introduction

1.1 The Bose gas

The behavior of bosonic particles at low temperatures is dominated by their tendency to occupy the lowest quantum energy state available. The phenomenon has been originally discussed for non-interacting Bosons, that is, for an *ideal Bose gas*, which undergoes a phase transition at low temperatures forming a Bose-Einstein condensate (BEC) of particles all of which occupy the same lowest energy state. At zero temperature all particles in the system are Bose condensed. The phenomenon is usually discussed in textbooks of statistical physics, which typically use the example of atoms confined in a box or that of a three-dimensional (3D) infinite system.

The efforts to realize in the laboratory a system which undergoes Bose condensation in the originally proposed sense concluded successfully in 1995 [1–3]. The system consists of a small number of alkali-metal atoms which varies between $N = 10^4$ and $N = 10^7$, and these are trapped by a confining potential. Atomic BECs are extremely dilute gases with dimensions in the range 1-100 μm and densities on the order of 10^{13} atoms/cm^3. The low densities mean that the atoms are interacting very weakly. The confining potential is created by either a magnetic field or a laser or by both, and it typically is a harmonic one in all three dimensions. Potentials of various forms are now possible (e.g., an anharmonic one [4]), and one may also generate potentials of various shapes [5]. The confining potential has two significant consequences concerning our understanding of a BEC. First, the condensation of atoms in the lowest energy state implies that these are localized around the minimum of the potential, i.e, it implies a condensation in space. Second, the boundaries of the system are set by the trapping potential itself, thus indicating a unique choice for well-defined boundary conditions in the system modelling.

[a] e-mail: komineas@pks.mpg.de

A primary method for the understanding of the dynamical features of a BEC is the study of its elementary excitations. Lieb and Liniger [6] employed the Bethe ansatz to obtain an exact diagonalization of the model Hamiltonian that describes a one-dimensional (1D) Bose gas interacting via a repulsive δ-function potential. Based on this solution Lieb [7] proposed an intriguing dual interpretation of the spectrum of elementary excitations, either in terms of the familiar Bogoliubov mode, or in terms of a certain kind of a particle-hole excitation which will hereafter be referred to as the Lieb mode. The energy-momentum dispersions of the Bogoliubov and the Lieb modes coincide at low momenta, where they both display the linear dependence characteristic of sound-wave propagation in an interacting BEC, but the Lieb dispersion is significantly different at finite momenta where it exhibits a surprising 2π periodicity.

The above subject re-emerged in connection with the soliton calculated analytically within a 1D classical nonlinear Schrödinger (NLS) model [8] while Zakharov and Shabat developed inverse-scattering techniques for the study of multisolitons [9]. Interestingly, the elementary soliton was later shown to provide an approximate but fairly accurate description of the quantum Lieb mode for practically all coupling strengths [10,11].

The same solitons motivated experimental observation of coherent structures in trapped BECs. The technique used in the first experiments was based on the observation that the soliton solution of the NLS presents a phase difference of the complex field across the axis. A phase difference of the condensate wavefunction was engineered between the two ends of the trap by using laser pulses in experiments employing an elongated [12] and a spherical trap [13]. A soliton was spontaneously created and was observed as a notch in the condensate density. In further experiments solitons were observed to decay to solitary waves with a more complicated structure [14–16].

A theoretical investigation of solitary waves in the environment of a 3D trap would elucidate the experimental results. While the studies of a 1D Bose gas remain theoretical to a large extent, the results of 3D calculations would be very close to experimental realizations of a Bose gas. One should aim to identify all possible solitary waves as these are expected to have different forms depending on the system parameters and geometry. In the following we discuss important solitary wave solutions of the equations for the trapped Bose gas. We start with a *quasi-1D soliton* in the trapped BEC which is related to the soliton of the 1D NLS. We further proceed to discuss vortex lines which are expected to exist in the quantum fluid under study. In particular, we discuss extensively *vortex ring* solutions which are propagating solitary waves in the condensate.

1.2 The Gross-Pitaevskii model

In a dilute Bose gas at very low temperatures the most significant interactions are collisions between pairs of atoms. Such interactions can be modelled by a pseudopotential in the form of a delta function. These ideas were exploited by Gross [17,18] and Pitaevskii [19] who proposed the description of a BEC by a single wavefunction (a complex field). This will be called the *condensate wavefunction* and it satisfies the Schrödinger equation with the addition of a nonlinear term which is due to scattering processes between pairs of atoms. For trapped condensates the Gross-Pitaevskii (GP) model has the form

$$i\hbar \frac{\partial \Psi}{\partial t} = -\frac{\hbar^2}{2M} \Delta\Psi + V_{\rm ext}\, \Psi + \frac{4\pi\hbar^2 a_s}{M} |\Psi|^2 \Psi, \tag{1}$$

where Δ denotes the Laplacian, M is the atom mass, and a_s denotes the scattering length which is a measure of the atom-atom interactions. The external potential $V_{\rm ext} = V_{\rm ext}(\boldsymbol{r})$ is usually assumed to be harmonic, as this is an accurate model for current experiments. We will typically consider an axially symmetric potential with axis of symmetry the z-axis:

$$V_{\rm ext}(\rho, z) = \frac{1}{2} M (\omega_\perp^2 \rho^2 + \omega_\parallel^2 z^2), \tag{2}$$

where (ρ, z) are cylindrical coordinates with $\rho \equiv \sqrt{x^2 + y^2}$, and $\omega_\perp, \omega_\parallel$ are the corresponding trapping frequencies. Other forms of trapping potentials, e.g., a quartic one, are possible to

realize experimentally and may be interesting to study theoretically. The GP equation is an excellent model for the description of dilute atomic BECs as has become evident by the very good agreement between numerous experiments and the corresponding theory in the last years.

The geometry of the system, that is, the form of the confining potential will largely define its detailed properties. In this respect it is important to note that the system parameters, that is, the trapping frequencies and the density of the condensate can be experimentally tuned in a wide range. In the present paper we focus attention to an elongated (cigar-shaped) trap for which $\omega_\parallel \ll \omega_\perp$. In order to simplify the discussion of travelling wave solutions, which will be studied in the following, we employ the approximation of an infinitely-elongated trap [20,21], that is, we set $\omega_\parallel = 0$ in Eq. (2). In other words, we suppose a constant linear particle density along the axis of the condensate.

Eq. (1) is most conveniently studied after we introduce rationalized units. We choose the oscillator length in the transverse direction $a_\perp \equiv (\hbar/M\omega_\perp)^{1/2}$ as the unit of length, while the natural time unit is $1/\omega_\perp$. We also define the corresponding oscillator length in the longitudinal direction $a_\parallel \equiv (\hbar/M\omega_\parallel)^{1/2}$ for future reference. Complete specification of the system requires as input the linear particle density n_1 which is the number of atoms per unit length of the cylindrical trap. This is equal to the integral $n_1 = \int \Psi^* \Psi dxdy$ in the transverse trap directions. The new units are implemented by applying the following rescalings in Eq. (1):

$$t \to \frac{t}{\omega_\perp}, \qquad \boldsymbol{r} \to a_\perp \boldsymbol{r}, \qquad \Psi \to \frac{n_1^{1/2}}{a_\perp}\, \Psi. \tag{3}$$

A further simplification of the model is achieved when we look for stationary wavefunctions. These can be found by the substitution $\Psi(\boldsymbol{r},t) \to \Psi(\boldsymbol{r})\, e^{i\mu t}$, where μ is the chemical potential. The GP equation then takes the form

$$i\,\frac{\partial \Psi}{\partial t} = -\frac{1}{2}\,\Delta\Psi + \frac{1}{2}\,\rho^2\,\Psi + 4\pi\,\gamma\,|\Psi|^2\,\Psi - \mu\,\Psi. \tag{4}$$

The only free parameter in Eq. (4) is $\gamma \equiv n_1 a_s$ and it measures the strength of the interactions. Eq. (4) should be supplemented with the normalization condition for the wavefunction which, on account of the units (3), now reads $\int \Psi^* \Psi dxdy = 1$.

The GP model possesses an energy and Eq. (4) can be derived by varying the following energy functional which has been extended to include the chemical potential:

$$W = \int \left[\frac{1}{2}\,(\boldsymbol{\nabla}\Psi^* \cdot \boldsymbol{\nabla}\Psi) + \frac{1}{2}\,\rho^2\,\Psi^*\Psi + 2\pi\,\gamma\,(\Psi^*\Psi)^2 - \mu\,\Psi^*\Psi\right] dV. \tag{5}$$

The energy, as well as μ, are measured in units of $\gamma_\perp(\hbar\omega_\perp)$, where $\gamma_\perp \equiv n_1 a_\perp$ is a dimensionless constant.

The ground state $\Psi_0(\rho)$ of the condensate depends on the radial coordinate only, and it is found by choosing some $\mu \neq 0$ and looking for a non-vanishing time-independent Ψ. An analytic solution is only possible in two cases. In the limit of vanishing nonlinearity we obtain the quantum harmonic oscillator whose ground state is a gaussian function $\Psi_0(\rho, z) = 1/\sqrt{\pi}\, e^{-\rho^2/2}$, and the chemical potential is $\mu = 1$. In the limit of strong nonlinearity ($\gamma \gg 1$) one can employ a Thomas-Fermi approximation [22] and disregard the Laplacian in Eq. (4) thus obtaining a particle density $|\Psi_0|^2 = (\mu - V_{\rm ext})/(4\pi\gamma)$. In the case of a harmonic potential this gives

$$\Psi_0 = \left[\frac{2}{\pi R_\perp^2}\left(1 - \frac{\rho^2}{R_\perp^2}\right)\right]^{1/2} \tag{6}$$

for $0 \leq \rho \leq R_\perp \equiv 2\gamma^{1/4}$, and $\Psi_0 = 0$ for $\rho > R_\perp$. The chemical potential is determined by the normalization condition and is given by $\mu = 2\,\gamma^{1/2}$. Finally, in the general case of an arbitrary γ the ground state wavefunction can only be calculated numerically.

2 Dark solitons

The GP equation describes not only the wavefunction in the ground state but also excitations of a BEC. In the following we discuss nonlinear excitations which are solitary wave solutions of the equation. These are interesting solutions as they are stationary states of the system. They should play an important role in the condensate dynamics and they are expected to be robust under collisions. They are further expected to play a role in the thermodynamics of the condensate.

We suppose that solitary waves are travelling along the z axis with a constant velocity v. The three-dimensional problem is somewhat simplified if we assume that some of the interesting solutions will preserve the axial symmetry of the trap [20,21]. These are described by a wavefunction of the form $\Psi = \Psi(\rho, \xi)$, with $\xi \equiv z - vt$, which is inserted in Eq. (4) to yield the stationary differential equation

$$-i\,v\,\frac{\partial \Psi}{\partial \xi} = -\frac{1}{2}\,\Delta\Psi + \frac{1}{2}\,\rho^2\,\Psi + 4\pi\,\gamma\,(\Psi^*\Psi)\,\Psi - \mu\,\Psi. \tag{7}$$

The wavefunction must vanish in the limit $\rho \to \infty$, thanks to the transverse confinement, while the condition

$$\lim_{\xi \to \pm\infty} |\Psi(\rho, \xi)| = |\Psi_0(\rho)| \tag{8}$$

enforces the requirement that the local particle density coincide asymptotically with that of the ground state Ψ_0. The phase of the wavefunction is not fixed *a priori* at spatial infinity but we assume von Neumann boundary conditions

$$\lim_{\xi \to \pm\infty} \frac{\partial \Psi}{\partial \xi} = 0. \tag{9}$$

If one neglects the transverse (ρ) degree of freedom, then Eq. (7) may be reduced to the nonlinear Schrödinger equation which has soliton solutions in one spatial dimension. Effective 1D models have been developed (see, e.g., [23]) and the relevance of the, so-called, dark soliton for a BEC was studied [24–30]. The soliton is found to be stable only in traps with a low enough density [26,28].

Solitary wave solutions of the full 3D Eq. (7) can only be found numerically. A Newton-Raphson method is employed in Refs. [20,21] and steady-state solutions were found. To apply this, the wavefunction is discretized on a numerical grid in the (ρ, z) space. The resulting set of equations is nonlinear and it is solved iteratively by a generalized minimal residual method. The algorithm needs an initial input configuration but most choices will only converge to the ground state. It is thus essential to provide the algorithm with an educated guess for the initial input configuration which then converges after a few iterations to a solitary wave solution. An obvious choice is given by the product ansatz

$$\Psi_{\rm in} = [c_1 - i\,c_2 \tanh(c_3 \xi)]\,\Psi_0(\rho), \tag{10}$$

which capitalizes on the analytically known solitary wave in the 1D model [8,9] which is multiplied by the ground-state configuration $\Psi_0(\rho)$. The latter can simply be chosen to be a gaussian or the Thomas-Fermi solution. The constants c_1, c_2 and c_3 are definite functions of the velocity v within the strictly 1D model, but could be used here as trial parameters until convergence is achieved. The converged configuration does not depend on the precise choice of those parameters, and it is certainly not in the form of a product ansatz often employed for the derivation of effective 1D models [25,29]. Finally, we note that the ansatz (10) satisfies the parity relation

$$\Psi(\rho, -\xi) = \Psi^*(\rho, \xi), \tag{11}$$

which is compatible with Eq. (7) and is actually satisfied by all solutions which will be discussed in the present paper.

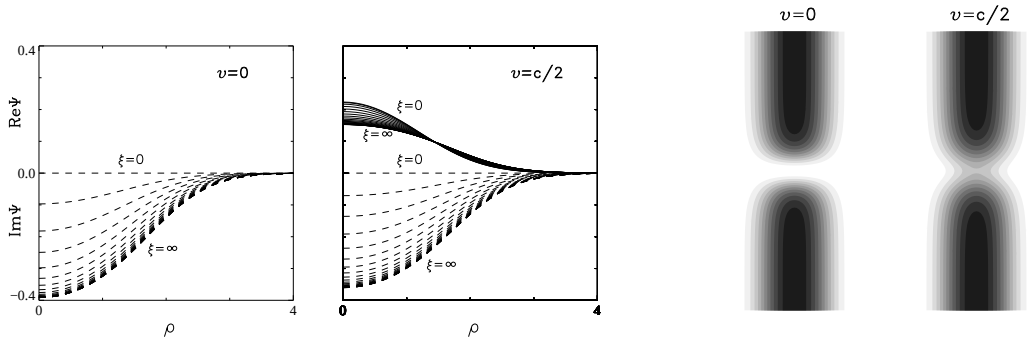

Fig. 1. Solitary wave at $\gamma = 1$ and two representative values of the velocity, $v = 0$ and $v = 0.45(\approx c/2)$. The two entries on the left display the radial dependence of the real (solid line) and the imaginary part (dashed line) of the wavefunction for various positive values of ξ in steps of $\delta\xi = 0.2$. The curves which correspond to the soliton center ($\xi = 0$) and away from the soliton center ($\xi = \infty$) are labelled. The corresponding results for negative ξ are obtained through the parity relations (11). The two entries on the right display contour levels of the corresponding local particle density $n \equiv |\Psi|^2$. The plane shown contains a [-6,6] portion of the z axis and cuts across the cylindrical trap. The complete 3D picture may be envisaged by simple revolution around the vertical (z) axis. Regions with high particle density are dark while regions with zero density are white.

In the present section we study the case of weak coupling, and we typically use an interaction strength $\gamma = 1$. In the numerical calculation it is probably simplest to employ the ansatz (10) with $c_1 = 0, c_2 = 1 = c_3$ and thus find the black soliton with velocity $v = 0$. Its wavefunction has a nontrivial imaginary part but vanishing real part, in view of the specific overall phase convention adopted in Eq. (10). The velocity is treated as a parameter in Eq. (7) and can be incremented in steps of, say, $\delta v = 0.01$, so that the complete family of dark solitons is calculated. The soliton velocities lie in the range $0 \leq v < c$ where $c = 0.95$ is the velocity of sound for the present parameters [21]. An equivalent sequence of solitary waves with velocities in the range $-c < v \leq 0$ is obtained by taking the complex conjugate of the wavefunction calculated for $0 \leq v < c$, since

$$v \to -v, \quad \Psi \to \Psi^* \,, \tag{12}$$

is an obvious symmetry of Eq. (7).

A detailed illustration of the calculated solitary wavefunction is given in Fig. 1 for two representative values of the velocity, $v = 0$ and $v = c/2$. The two entries on the left in the figure show the corresponding wavefunctions in the transverse (ρ) and axial (ξ) directions. A partial but more transparent illustration is given in the two entries on the right in the figure which depict the level contours of the local particle density $n \equiv |\Psi|^2$ for the same wavefunctions. In words, the calculated solitary wave reduces to a soundlike pulse that is a weakly nonlinear disturbance of the ground state when $|v|$ approaches the speed of sound c, while it becomes an increasingly dark soliton with decreasing $|v|$ and reduces to a completely dark (black) soliton at $v = 0$.

It is now important to calculate the energy-momentum dispersion of the solitary wave. The excitation energy is defined as

$$E = W - W_0, \tag{13}$$

where both W and W_0 are calculated from Eq. (5) applied for the solitary wave $\Psi(\rho, \xi)$ and the ground state $\Psi_0(\rho)$, respectively. The presence of the chemical potential in Eq. (5) is essential and it accounts for the fact that a solitary wave carries a different number of particles than the uniform ground state.

The usual definition of the linear momentum is

$$\mathcal{P} = \frac{1}{2i} \int \left(\Psi^* \frac{\partial \Psi}{\partial z} - \frac{\partial \Psi^*}{\partial z} \Psi \right) \, dV = \int n \, \frac{\partial \phi}{\partial z} \, dV, \tag{14}$$

and is measured in units of $\hbar n_1 = \gamma_\perp(\hbar/a_\perp)$. In the second step of Eq. (14) we employ hydrodynamic variables defined from

$$\Psi = \sqrt{n}\, e^{i\phi}\,, \tag{15}$$

where $n \equiv |\Psi|^2$ is the local particle density and the phase ϕ may be used to construct the velocity field $\boldsymbol{u} = \boldsymbol{\nabla}\phi$. In connection with the soliton in the 1D Bose gas it was noted that the definition of the linear momentum should be modified [10,11] due to the non-differentiability of the ordinary momentum $\mathcal{P}$ [31]. In the present case, of a 3D cylindrical condensate, the relevant physical momentum is the *impulse* Q [20] defined in a manner analogous to the case of a 1D gas:

$$Q = \int (n - n_0)\, \frac{\partial \phi}{\partial z}\, dV = \mathcal{P} - \delta\phi\,, \tag{16}$$

$$\delta\phi \equiv \int_0^\infty 2\pi\rho\, d\rho\; n_0(\rho)[\phi(\rho, z{=}\infty) - \phi(\rho, z{=}-\infty)]\,,$$

where $n_0 \equiv |\Psi_0(\rho)|^2$ is the ground-state particle density and $\delta\phi$ is now the weighted average of the phase difference between the two ends of the trap. The delicate distinction between linear momentum and impulse has been the subject of discussion in practically all treatments of classical fluid dynamics [32,33] and continues to play an important role in the dynamics of superfluids [34]. The validity of the definition of impulse in Eq. (16) is postulated since the corresponding group-velocity relation

$$v = \frac{dE}{dQ} \tag{17}$$

is satisfied in the numerical calculation and thus provides a highly nontrivial check of consistency. Needless to say, a relation of the form (17) would not be satisfied by the standard linear momentum (14). We finally note that the asymptotic values of the phase of the wavefunction at infinity $\phi_\pm \equiv \phi(x, y, z = \pm\infty)$ are constants and depend only on the velocity v. This can be proven analytically for axially symmetric solutions and it is also true for non-axisymmetric numerical solutions [35]. Therefore the expression for the asymptotic phase difference in the definition of the impulse (16) reduces to

$$\delta\phi = \phi_+ - \phi_-\,, \tag{18}$$

it depends only on the velocity v and characterizes a solitary wave.

The dispersion $E{=}E(Q)$ for the complete sequence of solitary waves with velocities in the range $-c < v < c$ is illustrated in Fig. 2. The apparent 2π periodicity seems surprising but occurred also in the original calculation of a similar mode by Lieb [7] within a full quantum treatment of a 1D Bose gas interacting via a δ-function potential. The solitary wave discussed above for $\gamma = 1$ is essentially quasi-1D, in this weak coupling region, and its main features are indeed captured by an effective 1D model [36].

Experiments on solitons in a BEC have followed the first theoretical predictions. The technique used was inspired by the characteristic phase difference (18) of 1D soliton solutions which is actually a common feature of all BEC solitary waves which are discussed here. In the experiment of Ref. [12] an axially symmetric elongated trap was used with $\omega_\parallel/\omega_\perp = 1/30$. A homogeneous potential was applied on the one half of the condensate, in the long direction, thus generating a phase difference between the two condensate parts. This *phase engineering* technique created the initial condition for the subsequent spontaneous generation of localized excitations which were observed to travel with velocities smaller than the speed of sound. Their velocity was found to depend on the initial generated phase difference and they were thus identified with solitons. In order to make contact with the above theoretical results we need to know the value of the dimensionless parameter γ. This is actually equal to the number of atoms in the condensate in a slice of thickness a_s and this is easily calculated to be $\gamma \approx 7$ for the experiment in Ref. [12]. In a further experiment presented in Ref. [13] a nearly spherical condensate was used. A similar phase engineering technique was applied and propagating solitons were

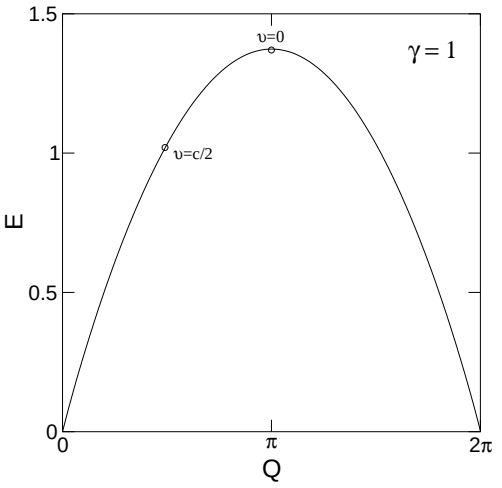

Fig. 2. Excitation energy E in units of $\gamma_\perp(\hbar\omega_\perp)$ vs impulse Q in units of $\gamma_\perp(\hbar/a_\perp)$ for $\gamma = 1$. The solitons illustrated in Fig. 1 are marked by circles. The black soliton ($v = 0$) lies at the curve maximum.

observed. Although the theoretical results presented above refer to infinitely-elongated traps, they can be modified and have indeed been applied to fully confined traps of various shapes including a spherical one [35,37].

3 Vortex rings

Interaction strengths in the atomic cloud larger than that considered in the previous section would lead to higher values of γ and thus to a stronger nonlinearity in Eq. (7). A qualitative change of the solitary waves is found numerically for values of $\gamma \geq 3$. While the form of the dispersion remains similar to that of Fig. 2 a part of the curve corresponds now to ring-like structures rather than to quasi-1D solitons. The ring structures will be called *vortex rings* since they are essentially closed vortex lines. Vortex rings resemble, roughly speaking, toroids where the condensate density is depleted. In particular, we have full atom depletion ($\Psi = 0$) on a circle whose axis is parallel to the axis of the condensate. In a full revolution around any point of the circle the phase of the condensate wavefunction changes by 2π, as is also the case for straight vortex lines, and thus the rings have a vortex character. In other words, we have a superfluid flow around the vortex ring.

For $3 \leq \gamma < 4$ the situation is the following. We have a black soliton for $v = 0$ ($Q = \pi$) while for finite velocity v smaller than some value $v_{\rm vr}$ ($0 < v \leq v_{\rm vr}$) we have vortex rings. The value of $v_{\rm vr}$ depends on γ and it increases as γ increases above the value $\gamma = 3$. For $v_{\rm vr} < v < c$ we still have quasi-1D dark solitons. The ring structure appearing for $0 < v \leq v_{\rm vr}$ is clear in the numerics but it is not pronounced since it appears near the flanks of the condensate where the density is low.

The situation described above signals a bifurcation which is reflected in the energy-momentum dispersion for $\gamma \geq \gamma_1 = 4$. We focus the discussion of the present section in the latter parameter regime where vortex rings play a central role. We choose $\gamma = 10$ and give the energy-momentum dispersion, which has now developed new features, in Fig. 3a. A fundamental solitary wave family (solid line) starts from $Q = 0$ where $v = c$, and $c = 1.77$ is the speed of sound. The curve reaches a maximum at $Q = 3.35$ and it turns to negative slope until $Q = 5.01$ where $v = -v_1$, and $v_1 = 0.84 = 0.47c$. The numerics do not give any continuation of this family for smaller values of the velocity $v < v_1$. Thus, this sequence of solitary waves has velocities in the range $-v_1 \leq v < c$. A corresponding sequence with $-c < v \leq v_1$ can be obtained through the symmetry relation (12), and it is a mirror symmetric of the original one around $Q = \pi$.

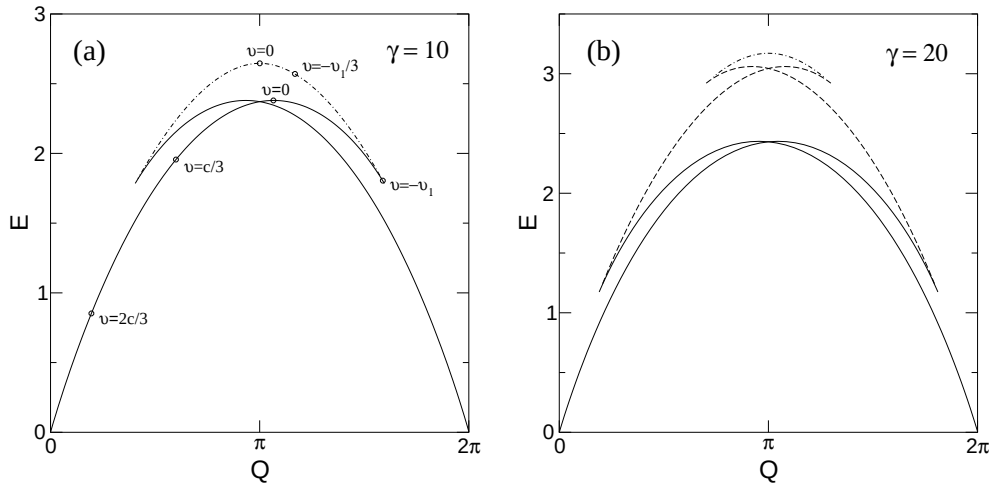

Fig. 3. Excitation energy E in units of $\gamma_\perp(\hbar\omega_\perp)$ vs impulse Q in units of $\gamma_\perp(\hbar/a_\perp)$. (a) $\gamma = 10$: the solid line corresponds to the fundamental sequence of vortex rings and the dashed-dotted line to the auxiliary sequence that contains the black soliton (at $v = 0$). The velocity of sound is $c = 1.77$ and the vortex ring velocity at the cusp is $v = -v_1 = -0.84$. (b) $\gamma = 20$: the additional dashed line corresponds to a sequence of double vortex rings.

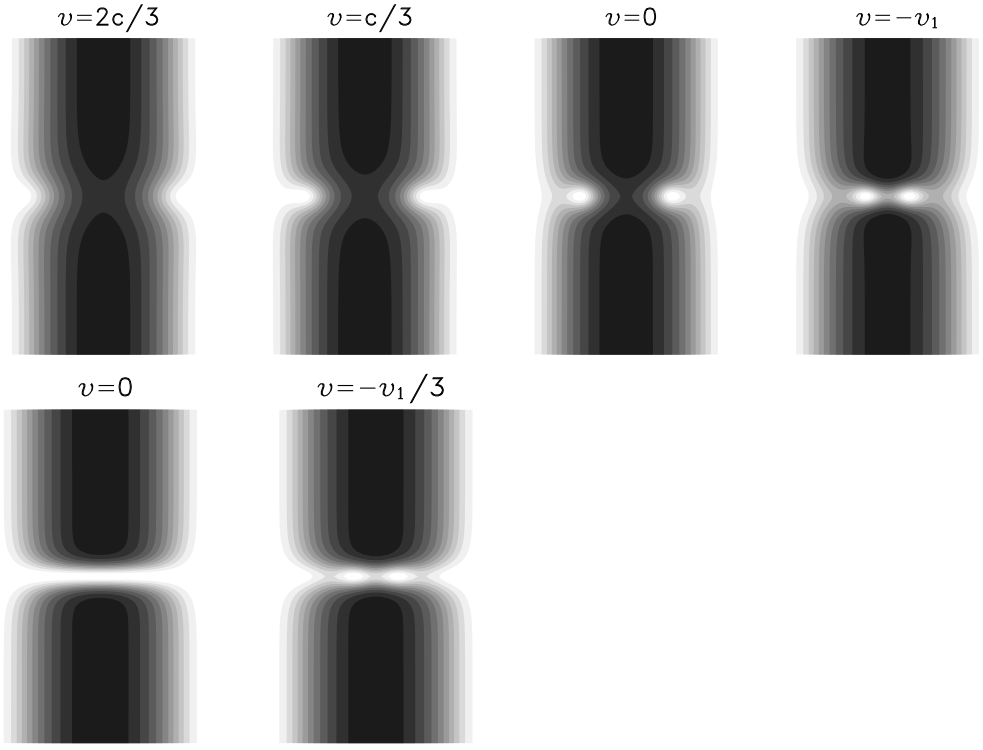

Fig. 4. Contour levels of the particle density $n \equiv |\Psi|^2$ for solitary waves for $\gamma = 10$ and some representative values of the velocity. The plane shown contains a [-6,6] portion of the z axis and cuts across the cylindrical trap. The complete 3D picture may be envisaged by simple revolution around the vertical (z) axis. Regions with high particle density are dark while regions with zero density are white. The four top entries correspond to points on the solid line in Fig. 3a. The two bottom entries correspond to points on the dash-dotted line in the same figure.

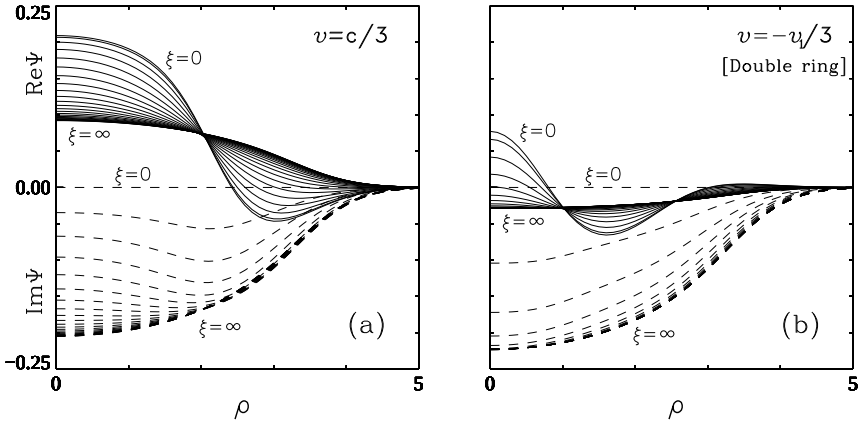

Fig. 5. (a) The full wavefunction for a vortex ring for $\gamma = 10$. It corresponds to velocity $v = c/3$ which is marked on the solid line in Fig. 3b. We show the radial dependence of the real (solid line) and the imaginary part (dashed line) of the wavefunction for various values of ξ in steps of $\delta\xi = 0.2$. The curves at the vortex ring central plane ($\xi = 0$) and away from it ($\xi = \infty$) are labelled. The corresponding results for negative ξ are obtained through the parity relations (11). (b) The full wavefunction for a double vortex ring for $\gamma = 10$. It corresponds to velocity $v = -v_1/3$ on the dashed-dotted line in Fig. 3a.

We turn to a description of the detailed nature of this new sequence of solitary waves. The dispersion is similar to that in Fig. 2 for velocities near the speed of sound, i.e., at low impulse Q. In this regime we have a quasi-1D soliton which appears as a weakly nonlinear disturbance of the ground state. A partial illustration of solitary waves is given in Fig. 4 where we depict the local particle density $n \equiv |\Psi|^2$ on a plane which contains the z axis and cuts across the cylindrical trap. A quasi-1D soliton at $v = 1.2(\approx 2c/3)$ is shown in the first frame on the top row. The dominant features of the solitary wave are pronounced as the velocity is decreased. For $v = 0.6(\approx c/3)$ (second frame, top row of Fig. 4) a ring structure has developed although this is not completely apparent in the partial illustration of the figure. The features of the vortex ring become completely apparent, and its radius is tightened, as we proceed to smaller values of the velocity. A notable special case is the static ($v = 0$) vortex ring which corresponds to a local maximum of the solid curve in Fig. 3a. The static vortex ring has radius $R = 1.8$ and it is illustrated in the third frame, top row of Fig. 4. If one considers a full revolution around the symmetry (vertical) axis of this figure, it is clear that the density near the center of the soliton ($\xi = 0$) vanishes on a ring.

One would think that pushing the velocity v to negative values would somehow retrace the calculated sequence of vortex rings backwards. In fact, the numerical algorithm continues to converge to vortex rings of smaller radii until the critical velocity $-v_1$ is encountered where the ring achieves its minimum radius $R_{\min} = 0.8$, and ceases to exist for smaller values of v. The terminal state at $v = -v_1$ is illustrated in the last frame, top row of Fig. 4.

The wavefunction of a vortex ring is completely illustrated through its real and imaginary parts in Fig. 5a for a representative value of the velocity $v = c/3$. Both the real and the imaginary part at the center of the soliton ($\xi = 0$) vanish for a specific radius $R = 2.4$, thus a ring structure emerges.

We have thus described a sequence of solitary waves which consists of bonafide 3D vortex rings. The corresponding branch in the energy-momentum dispersion of Fig. 3a is labelled by velocities $v = 2c/3$, $c/3$, 0, $-v_1$. As mentioned already, an equivalent sequence of solitary waves exists in the range $-c < v \leq v_1$ and leads to a dispersion curve in Fig. 3a that is mirror symmetric to the original branch around $Q = \pi$.

The black soliton is easily obtained numerically but it does not belong to the family denoted by the solid line in Fig. 3a. It is found at the maximum of an additional curve which is denoted by a dashed-dotted line in the same figure. The black soliton is static ($v = 0$) and its impulse is

$Q = \pi$. It is illustrated through its particle density in the first frame, bottom row of Fig. 4. The dashed-dotted line exists only over the limited velocity range $-v_1 < v < v_1$ and it is symmetric around $Q = \pi$. The part of the dotted line with $Q > \pi$ ($v < 0$) can be obtained from the part with $Q < \pi$ ($v > 0$) by using the symmetry relation (12). The dotted line joins smoothly with the solid lines at $Q = 5.01, 2\pi - 5.01$ forming cusps that correspond to $v = \pm v_1$. In fact, the two sequences terminate at precisely the same solitary wave at the cusps (shown in the last frame, top row of Fig. 4).

The solitary waves in the upper branch of the dispersion on either side of the black soliton are double vortex rings, that is, two nested vortex rings with a common axis of symmetry z. As one moves away from $v = -v_1$ on the dash-dotted line in Fig. 3 a second ring structure is nucleated at the flanks of the trap, while the original ring is preserved at constant radius $R = R_{\rm min} = 0.8$. The second ring moves to smaller radii as the velocity is descreased. The ring structure is tamed at the same time and the double vortex ring degenerates to a black soliton at $v = 0$. The particle density for a double ring with $v = -0.3 (\approx -v_1/3)$ is shown in the second frame, bottom row of Fig. 4. The outer ring structure is however not completely apparent in this partial illustration. The full wavefunction for the same vortex ring is shown in Fig. 5b. We have $\Psi = 0$ on two circles as inferred from the fact that the imaginary part of Ψ is zero for $\xi = 0$ while the real part is vanishing at two points along the coordinate ρ. The two coaxial vortex rings have opposite circulation, so that the phase difference is zero along any closed loop containing both rings.

Some of the features of the energy-momentum dispersion are sufficiently surprising to deserve closer attention. For example, simple inspection of Fig. 3a reveals that the group velocity becomes negative in the region $-v_1 \leq v < 0$ on the solid line or, equivalently, the impulse is opposite to the group velocity. This rotonlike behavior is consistent with the Onsager-Feynman view of a roton as the ghost of a vanished vortex ring [38] because the calculated radius of the vortex ring is monotonically decreasing along the fundamental (solid line) sequence. A full-scale roton would develop if the terminal point $v = -v_1$ were an inflection point beyond which the group velocity begins to rise again. Actually, this is exactly what happens as one moves away from point $v = -v_1$ along the upper branch in Fig. 3a, but this "roton" portion of the dispersion now appears in a strange location by comparison to the usual situation in liquid helium [38]. On the other hand, the black soliton at the stationary point $v = 0$ (dashed-dotted line) is indeed the ghost of a vanished vortex ring, as explained in the preceding paragraph. Needless to say, the rotonlike behavior described above is not directly connected with the Bogoliubov mode and thus should not be confused with the actual roton observed in liquid helium.

An essential feature of solitary waves is that the condensate density is significantly depleted near their core. The fluid loses completely its Bose-condensed character and it is normal at the core. The difference between the number of condensed atoms in a solitary wave and those in the ground state of a cylindrical condensate $M = N - N_0$ can be considered as a mass deficit carried by the solitary wave. This mass deficit (henceforth called simply *mass* of a solitary wave) is plotted in Fig. 6 for vortex rings and solitons for $\gamma = 10$. The negative value of the mass indicates that this is actually a mass deficit and this is not symmetric around $v = 0$ contrary to what one might expect. It actually acquires a minimum at $v = 0.1$. A mirror image of the curve around $v = 0$ can be obtained by the symmetry relation (12). The solid and the dashed-dotted lines in Fig. 6 join at a point which corresponds to the cusp in Fig. 3a (at $v = -v_1$). We note that the numerical results are compatible with $dM/dv \to \infty$ at $v = -v_1$, as is also apparent in the figure.

The solitary wave dispersions become increasingly more complicated with increasing values of the dimensionless coupling constant γ. Numerical calculations reveal yet another critical coupling $\gamma_2 \approx 12$, in the sense that new flavor arises for $\gamma > \gamma_2$. The structure of the solitary waves in this new regime becomes sufficiently clear for $\gamma = 20$ and is best summarized by the calculated energy-momentum dispersion shown in Fig. 3b. Apart from mirror symmetry, the dispersion now exhibits two cusps that correspond to two critical velocities $v_1 = 1.35 = 0.64c$ and $v_2 = 0.48 = 0.23\,c$, where $c = 2.1$ is the speed of sound for $\gamma = 20$ [21].

The nature of the solitary waves associated with the various branches in the dispersion of Fig. 3b is very briefly described in the following. The lowest branch (solid line) corresponds to

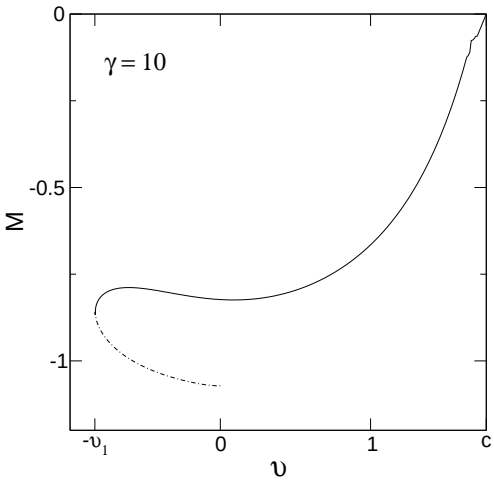

Fig. 6. The mass M in units of $\gamma_\perp$ as a function of the solitary wave velocity v for $\gamma = 10$. The mass is negative (which actually indicates a mass deficit) and has a minimum at $v = 0.1$. The solid line corresponds to the sequence of vortex rings (solid line) in Fig. 3, and the dashed-dotted line corresponds to the dashed-dotted line in the same figure.

single vortex rings with velocities in the range $c > v \leq -v_1$, as in the case $\gamma = 10$. Again the ring achieves its minimum radius at the critical velocity $v = -v_1$ at the cusp between the solid and the dashed lines. The intermediate branch (dashed line) corresponds to double rings with velocities in the range $v_2 \leq v \leq -v_1$. The second ring is first created at the flanks of the trap and comes closest to the original ring at the new critical velocity $v = v_2$ at the cusp between the dashed and the dashed-dotted lines. One more ring is nucleated at the upper branch (dashed-dotted line) which corresponds to triple rings, with velocities in the range $0 < v < v_2$. The ring structures gradually fade away to become a black soliton at $v = 0$, at the maximum of the dashed-dotted curve.

While the numerical calculation becomes increasingly more difficult for larger values of γ, it is clear that a sequence of critical couplings $\gamma_1, \gamma_2, \ldots$ exists and leads to a hierarchy of axisymmetric vortex rings.

In the theory described above we have supposed that the trap is infinitely-elongated, that is, we chose a longitudinal trapping frequency $\omega_\parallel = 0$. Steady state solitary wave solutions are certainly not possible in finite traps, however, we expect that the features of vortex rings described above are preserved for sufficiently elongated traps with $\omega_\parallel \neq 0$. A special example is the static vortex ring solution. This exists as an exact solution also in finite traps [37]. Static black soliton solutions exist in practically any trap geometry, while the bifurcation from a soliton to a vortex ring solution has also been studied [37].

An experimental realization of vortex rings in an almost spherical trap was presented in Ref. [14]. The technique used created a full depletion of the condensate across its middle plane combined with an induced phase difference π between the two condensate parts. This technique initially created a dark soliton which subsequently decayed into a vortex ring.

A different technique was used in the experiments of Ref. [15]. A light pulse propagating along an elongated condensate was compressed to a few micrometers using the slow-light technique, and this subsequently created a density defect in the condensate. The latter developed in a series of solitons of which the most pronounced one decayed to vortices. These vortices were reported to have a complicated 3D structure and the experimental pictures are indeed similar to 2D projections of vortex rings like the ones shown in Fig. 4. They were also observed to propagate in the condensate in agreement with vortex ring properties discussed in this section.

The decay of solitons to vortex rings, which is common in the two aforementioned experiments, had been previously predicted by solving the corresponding initial value problem in a 3D GP model [28]. The same instability in a trapped condensate can readily be inferred by

the form of the energy-momentum dispersions in Figs. 2, 3. The curve in Fig. 2 has a single maximum which corresponds to a black (static) soliton, while in Fig. 3 a second maximum has been born which corresponds to a static vortex ring. This indicates a bifurcation of static solitary waves ($v = 0$) which actually occurs at $\gamma = 4$ [35]. The quasi-1D soliton should naturally turn unstable at the bifurcation. A complete stability analysis for the soliton would be needed in order to establish its regime of stability [26,28]. This issue will not be discussed in detail in this paper, except for brief comments contained in the concluding section.

Vortex rings in a homogeneous Bose gas have been previously studied in a well-known paper by Jones and Roberts (JR) [34]. The solutions of the GP model in a 3D infinite system were given only numerically but their main features are sufficiently simple to allow comparison with vortex rings in a trapped gas. As with ordinary smoke rings in fluid dynamics, the JR rings cannot be static. The latter property can be proven using a virial relation which prevents finite-energy solutions with $v = 0$ in the homogeneous GP model. As a result, the radius of the vortex ring grows to infinity at low velocity. This picture is completely rearranged in a cylindrical trap because the occurrence of slow vortex rings with large radius is restricted by the boundaries of the trap. Instead, vortex rings are predicted to nucleate at the flanks of the trap as soundlike pulses with high velocity approaching the speed of sound c, while their radius actually decreases with decreasing velocity. In particular, it is now possible to obtain static ($v = 0$) vortex rings of finite radius that are no longer contradicted by any virial relation. The structure of the energy-momentum dispersion in Fig. 3 clearly reflects the substantial restructuring of vortex rings within a cylindrical trap.

A further important feature of vortex rings in a cylindrical trap is the characteristic phase difference Eq. (18) of their wavefunction between the two ends of the trap. The corresponding phase difference for the JR rings is zero which is consistent with the fact that they have a finite energy; any nonzero phase difference (18) in the infinite 3D system would result in a diverging energy of the vortex rings.

It is then natural to question whether or not there exists a limit in which the JR vortex ring is recovered. One should expect that this may happen when the bulk healing length $(8\pi na)^{-1/2}$ is significantly smaller than the transverse confinement width. This limit is translated into large values of γ which is the only dimensionless parameter that enters the rationalized GP equation. Now, our discussion earlier in this section suggests an increasingly complicated hierarchical structure in the strong-coupling limit rather that a simple JR soliton. A part of the dispersion (e.g., in Fig. 3) might correspond, in the appropriate limit, to the JR rings but this cannot be directly inferred from the present discussion.

4 Collisions between solitary waves

The intriguing features of solitons and vortex rings in a trapped BEC which were discussed in detail in Sects. 2, 3 indicate that this an excellent physical system for the study of dynamical properties of nonlinear waves. The experiments [12–15] which were briefly described in the two previous sections show that a number of experimental techniques are available for the controlled generation of practically all types of solitary waves and for the subsequent observation of their dynamics. In a recent experiment by Ginsberg *et al* [16] interactions among solitary waves were observed. The experimental technique employed which was an extention of that used in [15] where compressed light pulses induce density defects in the condensate. Nonlinear excitations are then created and they collide against each other. While solitons and vortex rings were robust in many collision events, in some cases shell structures of low particle density were observed, which had not been predicted before. Those and other compound structures observed should apparently be studied in their own right [39].

In the present section we discuss interactions, in particular head-on collisions, between the solitary waves which were presented in the last two sections. These are important in order to understand the mechanisms of their creation and annihilation and also for the understanding of other types of excitations in a BEC like those observed in the experiments of Ref. [16]. Interactions between vortices or vortex rings [40] are also important for the understanding of superfluid turbulence [41].

In the 1D nonlinear Schrödinger equation, which describes the 1D Bose gas, soliton collisions are elastic, that is no energy is radiated and the outgoing solitons are the same as the colliding ones [42]. In the homogeneous 3D Bose gas, solitary waves have the form of vortex rings or rarefaction pulses [34]. In contrast to the 1D case, collisions are generally inelastic. Large vortex rings annihilate when they collide head-on by increasing their radius and radiating phonons [43, 44].

We focus here on head-on collision dynamics of solitons and vortex rings in a cylindrically confined BEC. This system interpolates between 1D and 3D solitary waves since it supports excitation modes which are hybrids of solitons and vortex rings. The numerical simulations will use the GP model

$$i\,\frac{\partial \Psi}{\partial t} = -\frac{1}{2}\,\Delta\Psi + \frac{1}{2}\,\rho^2\,\Psi + 4\pi\gamma\,|\Psi|^2\Psi. \tag{19}$$

This is written in a dimensionless form and differs from Eq. (4) only in that it now does not assume a constant chemical potential μ. We consider the time evolution given by Eq. (19) ane we choose as an initial condition two solitary waves with opposite velocity which are initially well separated from each other. We denote by $\Psi_{SW}(\rho, z; v)$ the wavefunction of an axially symmetric solitary wave travelling with velocity v, like the ones discussed in the previous sections. We aim to simulate head-on collisions and we thus make an appropriate two-soliton ansatz which we choose as

$$\begin{aligned} \Psi(\rho, z) &= \Psi_{SW}(\rho, z - \frac{d}{2};\, v), \quad \text{if } z < 0 \\ \Psi(\rho, z) &= \Psi_{SW}(\rho, z + \frac{d}{2};\, -v), \quad \text{if } z \geq 0, \end{aligned} \tag{20}$$

where d is a constant and gives the distance between the solitary waves. For a solitary wave with velocity $-v$ we will typically choose the wavefunction given by the symmetry relation (12). The ansatz represents two solitons centered around $z = \pm d/2$ which are in a head-on collision course. We confine ourselves to the case of solitons having equal and opposite velocities. The distance d will be chosen large enough so that the two solitons are well separated. In that case Ψ has a well defined modulus for $z \to 0^{\pm}$. A phase can be chosen arbitrarily for each one of the two parts of the wavefunctions at $z < 0$ and $z \geq 0$ in (20), and it is thus possible to arrange that the phase of Ψ is continuous at $z = 0$. Let us suppose that Ψ has a phase, say, ϕ_0 at $z \to -\infty$. This changes by $\delta\phi$, which depends on v, as $z \to 0$ and it subsequently changes by $-\delta\phi$ back to the value ϕ_0 at $z \to \infty$.

Eq. (19) has been integrated numerically for various values of the parameter γ and for the full range of solitary wave velocities [45]. The lattice used is typically 6×60 in the (ρ, z) plane. The boundary condition at the ends of the lattice in the z-direction is $\partial\Psi/\partial z = 0$. This results in reflection of waves when these reach the boundaries during the course of the simulation. In full 3D simulations one observes that the axially symmetry of the initial wavefunction is preserved throughout the process. The numerical simulations are then significantly accelerated if one assumes axial symmetry in the algorithm as is the case for the simulations presented in this section.

4.1 Collisions between quasi-1D solitons

We start from the quasi-1D case by choosing a small value for $\gamma = 1$. The initial condition in the simulations is two quasi-1D solitons of the type discussed in Sect. 2. In Fig. 7a we present five snapshots of the simulation for solitons with initial velocity $v = 0.2(0.21c)$. The solitons decelerate as they approach and interact, they reach a minimum separation and finally bounce back. This behavior is typical for small velocities. As the velocity of the initial solitons increases, they pass through each other during collision as is seen in Fig. 7b for $v = 0.6(0.63c)$. One finds that the outgoing solitons after collision are, for all values of the velocity v, very similar to the incoming ones and no visible radiation is produced, thus collisions are elastic.

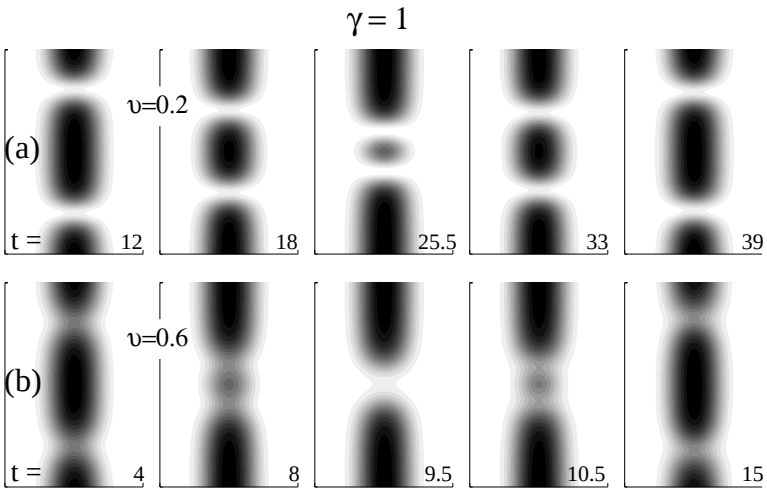

Fig. 7. Plots of the particle density $n \equiv |\Psi|^2$ for quasi-1D soliton collisions on a scale from white at zero to black at maximum density for each plot. Each row shows five snapshots of a collision at $\gamma = 1$, and velocities v as indicated. The time t for each snapshot is shown on the figure. The plane shown contains a [-6,6] portion of the z axis and cuts across the cylindrical trap. The initial separation (at $t = 0$) of the solitary waves is $d = 12$ in units of $a_\perp$ for all cases.

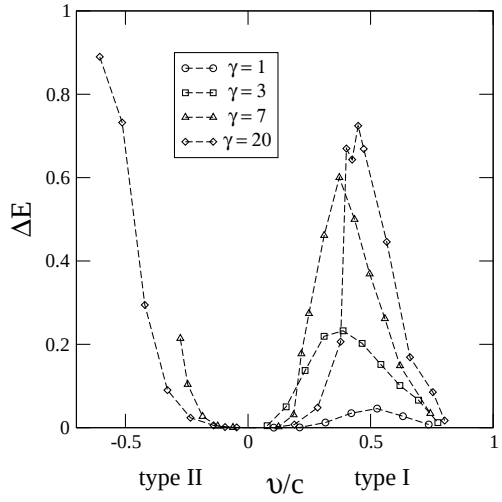

Fig. 8. The energy fraction ΔE, defined in Eq. (21), which is radiated during collision of solitons and vortex rings as a function of their initial velocity, for four values of the coupling constant γ. Type I vortex rings are presented at positive values of the velocity and type II vortex rings at negative velocities. The velocity is normalized to the speed of sound $c = 0.95, 1.29, 1.61, 2.1$ (in units of $a_\perp \omega_\perp$) for $\gamma = 1, 3, 7, 20$, respectively. The symbols correspond to the simulations performed.

A measure of the energy transformed to radiation during collision is given by

$$\Delta E = \frac{E_i - E_f}{E_i}, \tag{21}$$

where E_i is the energy of the incoming solitons and E_f is the energy of the outgoing ones. The energy E_f of the outgoing solitons is inferred by measuring their velocity well after the collision. As seen in Fig. 8, ΔE reaches a maximum 5% for intermediate velocities $v \approx 0.5c$.

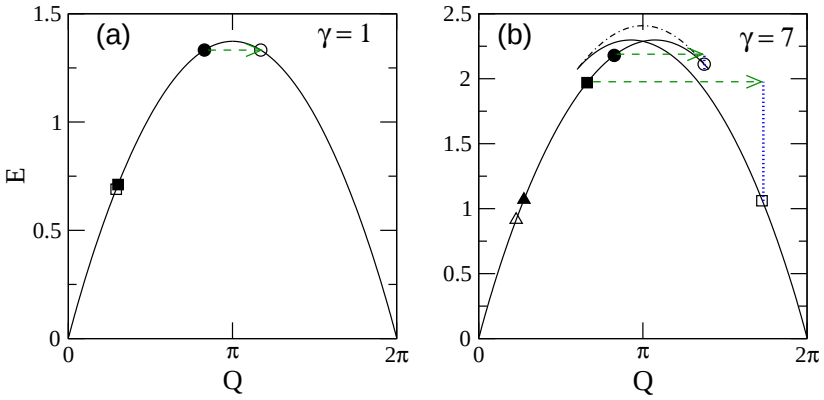

Fig. 9. The excitation energy E versus impulse Q for solitary waves. (a) $\gamma = 1$: it corresponds to Fig. 2. (b) $\gamma = 7$: this is qualitatively similar to Fig. 3, and the velocity of vortex rings at the cusps is $|v| = v_1 = 0.3c$. The impulse transfer during bounce-off collisions is indicated by the dashed arrow connecting initial solitary waves (filled symbols, see text) with collision products (open symbols). The vertical dotted lines indicate the energy loss.

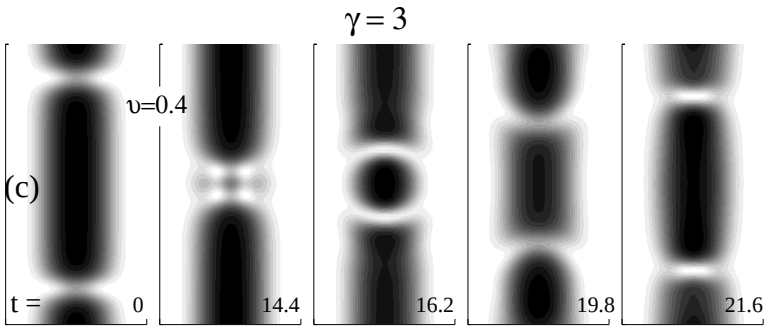

Fig. 10. Plots of the particle density $n \equiv |\Psi|^2$ for solitary wave collisions on a scale from white at zero to black at maximum density for each plot. We show five snapshots of a collision at $\gamma = 3$ and $v = 0.4$. The time for each snapshot is shown on the figure. The plane shown contains a [-8,8] portion of the z axis and cuts across the cylindrical trap. The initial separation (at $t = 0$) of the solitary waves is $d = 12\, a_\perp$.

The scattering behavior can be rationalized by using the dispersion diagrams which have been discussed in the previous sections and are now shown in Fig. 9. One of the initial solitons with $v = 0.21c$ is denoted by a filled circle in Fig. 9a, and it appears that it effectively moves along the dispersion curve due to the collision process to the point denoted by an open circle at almost the same energy level. This picture gives a precise result for the final outcome of the collision, and it also describes gross features of the collision process. It certainly does not give the detailed features of the process because the dispersion pertains only to isolated solitary waves. In the dispersion diagram of Fig. 9a, one of the solitons with $v = 0.63c$ is represented by a filled square before and by an open square after collision. The energy difference between the two points is small, thus the collision is almost elastic. The processes that we described above give a more or less complete account of the situation for small values of γ. The overall picture closely resembles the elastic soliton collisions in the integrable NLS [42]. We may thus say that the BEC behaves as a one-dimensional system as regards simple soliton dynamics for values of $\gamma \leq 2$.

The time evolution of soliton pairs described above suggests possible mechanisms for generating BEC solitons. One could consider the profile shown in the middle entry of Fig. 7b. This shows a dip in the condensate density while the condensate phase (not shown on the figure) is

nearly uniform. The subsequent evolution shown in the two last entries of Fig. 7b suggest the following: a full depletion of the density which may be induced in a dilute condensate could give rise to two solitons which would subsequently drift apart from each other. The above discussion and the examples of Fig. 7 suggest that the resulting solitons will be fast travelling ones. This picture is a particular case of the ideas developed within the inverse scattering transform [42]. Namely, an initial profile of the wavefunction will decay to solitons and linear waves. The solitons will be isolated after sufficiently long time. Furthermore, the linear waves can be avoided by a special choice of the initial wavefunction profile.

The simulations have been repeated for a larger interaction strength by setting $\gamma = 3$. Vortex rings, albeit with a very inconspicuous ring structure, form now part of the solitary wave family. The gross features of the picture described for $\gamma = 1$ survive here as well. For small velocities the solitons approach to a minimum distance and they bounce back. For a larger velocity they overlap during collision and pass through each other. Collisions for slow as well as for fast solitary waves are also in this case elastic. The energy loss (21) can be calculated less accurately when $v \approx c$ because the energies of the initial and the final solitons E_i and E_f are small. We now observe that the energy radiated during collision reaches a maximum 23% at $v = 0.4c$ ($c = 1.29$) as shown in Fig. 8. In Fig. 10 we show five snapshots of the simulation for $v = 0.4(0.31c)$ which is close to the velocity where the behavior turns from bouncing back to passing through. The second snapshot shows the formation of fully fledged vortex rings at the time of collision. One can check that such conspicuous vortex ring structures do not exist as isolated solitary waves. The outgoing waves are seen to be of the soliton type in the fourth snapshot. However, these are later spontaneously transformed to depletion droplets, i.e., strongly localized regions of low density, as seen in the last snapshot. At later times not shown on the figure, the droplets transform into soliton-like structures and periodically revive two to three times until they reach the end of the numerical lattice. The speed of the wave is almost constant at $0.48c$.

4.2 Collisions between vortex rings

We further discuss how the picture is getting more interesting as the interaction strength γ increases. The energy-momentum dispersion for axially symmetric solitary waves changes substantially for $\gamma \geq \gamma_1 = 4$, and it is shown for $\gamma = 7$ in Fig. 9b. In the following we need to distinguish between the vortex rings on the left and those on the right of the dispersion maximum. We call the vortex rings with $0 < v < c$ type I, and those with $-v_1 \leq v < 0$ type II. The branch denoted by a dotted line in Fig. 9b will not be discussed further here.

An ansatz of the form (20) is used as an initial condition in simulations of head-on collisions of vortex rings. The two colliding vortex rings are identical except that they are moving in opposite directions. The energy radiated due to collision for a coupling constant $\gamma = 7$ is shown in Fig. 8. The maximum is now at 60% and occurs for an initial velocity $v = 0.37c, (c = 1.61)$. On the other hand, collisions at low and high velocities appear to be elastic, i.e., the outgoing solitary waves have almost the same energy as the incoming ones.

Fig. 11a shows the collision of vortex rings with an initial velocity $v = 0.3(0.19c)$. The initial rings are denoted by a filled circle in the dispersion (Fig. 9b) and they are type I. They reach a minimum distance, their radius decreases, and subsequently they bounce back. The outgoing rings are both type II, they still have the original circulation and are denoted by an open circle on the dispersion curve. The change in nature of the rings is apparent in the change of the ring radius between the first and last snapshots in Fig. 11a. The energy radiated during this process is 3%. It appears that each ring has effectively moved along one of the branches of the dispersion curve. This picture gives a precise result for the final outcome of the collision, but it also gives a faithful representation of the gross features throughout the collision process. The almost elastic collisions of slow vortex rings seen here are in stark contrast to collisions in the 3D bulk where vortex rings increase their radius and eventually annihilate [43].

One may also choose the initial vortex rings to be type II and still have initial velocity $|v| = 0.3(0.19c)$ as in Fig. 11b. In this case the collision causes them to increase their radius,

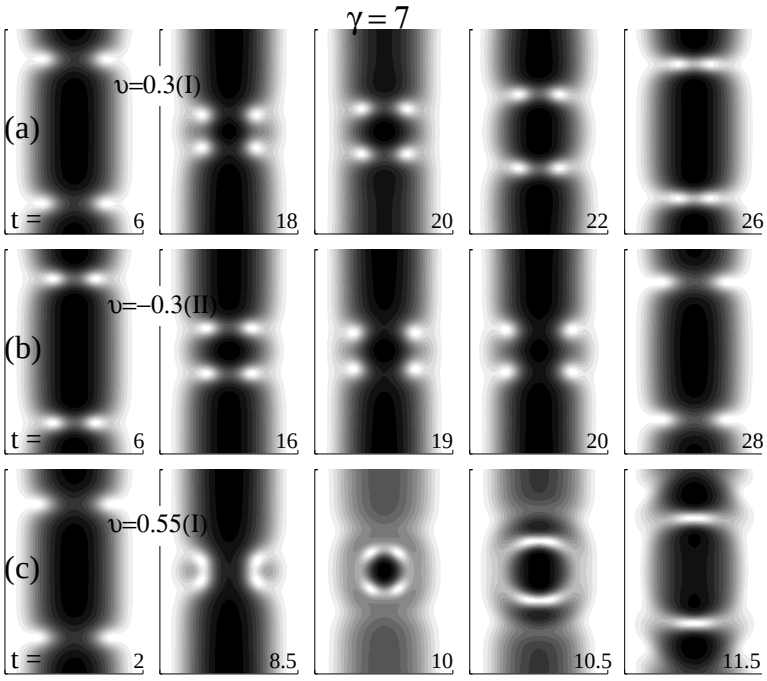

Fig. 11. Particle density $n \equiv |\Psi|^2$ for solitary wave collisions at $\gamma = 7$ for representative values of the velocity, shown on the figure. The gray scale ranges from white at zero to black at maximum density for each plot. The time for each snapshot is shown on the figure. The plane shown contains a [-6,6] portion of the z axis and cuts across the cylindrical trap. The initial separation of the solitary waves is $d = 12\, a_\perp$.

and they are eventually transformed to type I rings moving in opposite directions. The process is essentially the reverse of the one in Fig. 11a.

Kelvin [46] has considered the situation of a vortex ring in an ordinary fluid colliding on a surface. In an interesting comment [46] it is reported that he has studied the pressure exerted by a vortex ring, which is moving along a closed cylinder, upon the end surface of the cylinder. He predicted that, as the vortex ring approaches the cylinder surface, it will expand out and crawl back along the cylinder. The latter comment is in agreement with the situation presented in Fig. 11b. Kelvin further comments that there is a finite pressure exerted on the surface due to the vortex ring impulse. It would be interesting to study numerically or otherwise the pressure exerted by a vortex ring in view of the unusual definition of the vortex ring impulse given in Eq. (16).

We further consider collisions where the initial type I vortex rings have energy slightly lower than the energy at the cusp, as for example at the point denoted by a filled square in Fig. 9b (corresponding to $v = 0.5(0.31c)$). The bounce-back process of vortex rings cannot occur in this case. Instead, intermediate structures are formed, and the collisions are highly inelastic. In the example shown in Fig. 11c we have an initial velocity $|v| = 0.55$ $(0.34c)$ for type I rings. A shell-like object of low density is formed as the rings collide, which is seen in the third entry of the figure. Since the present simulations assume axial symmetry, the shell in the third entry of Fig. 11c is actually almost spherical, and thus strongly reminiscent of those observed in Ref. [16]. At later times in the simulation, after the collision, depletion droplets are formed which move away as shown in the last entry of the figure. These are similar to the ones reported in Fig. 10 for $\gamma = 3$, they travel coherently for a distance of approximately $10a_\perp$ and they eventually seem to decay into solitons. The depletion droplets are distinctly different than solitary waves theoretically studied in a confined BEC but they are reminiscent of rarefaction pulses in the homogeneous Bose gas [34].

The collision process is schematically shown on the dispersion diagram in Fig. 9b. One of the initial vortex rings is denoted by a filled square. Since it has no counterpart on the opposite side of the curve it emits radiation and is eventually transformed to a solitary wave with a much lower energy. The collision is highly inelastic in the sense that the main outgoing waves carry only part of the total energy while the rest of the energy is radiated away. However, it is possible that some of the remaining energy is carried by shallow gray solitons.

The spherical depletion shells reported here are produced by an elementary head-on collision process which is significantly simpler than the process reported in the experiment where many nonlinear wave structures interact simultaneously while the condensate is expanding. The resemblance between the observed structures suggests that inelastic collisions of axisymmetric nonlinear waves is the fundamental process underlying the generation of spherical waves observed experimentally [16].

We conclude the discussion of the $\gamma = 7$ case with solitary waves with v close to c. These have low energies and a dark-soliton character. They pass through each other during collision much like the situation for small couplings. In Fig. 9b the solitary wave with $v = 1.0(0.62c)$ is denoted by a filled triangle. After the collision it has only slightly lower energy (open triangle). Thus, collisions for large velocities are elastic as is also shown in Fig. 8.

We finally consider simulations of solitary wave collisions for higher values of γ. We choose $\gamma = 20$ which is the case presented in Fig. 3b where the nonlinear excitation spectrum is significantly complicated. Only the sequence of vortex rings on the solid curve of the figure will be considered. Collisions of vortex rings of type I are elastic for small as well as for large velocities in a manner similar to what has been discussed for smaller γ values. For intermediate velocities the energy loss (21) during collision is large and reaches over 70% for $v = 0.5c$. Vortex rings of type II collide elastically only for small velocities, while for larger velocities the initial vortex rings are destroyed during collision and the collision products are a mixture a many linear and nonlinear waves. In the simulation we typically identify the one which carries the largest mass depletion after collision. This carries an energy much smaller than that of the initial vortex rings and this is reflected to a large energy loss, close to 90% as shown in Fig. 8.

Fig. 8 shows that collisions are elastic for all couplings when the colliding solitary waves are slow or when they are dark solitons with a velocity close to the speed of sound. For intermediate velocities energy is radiated during collision and this is higher as the coupling increases.

Further conclusions concerning the case of bouncing-back vortex rings can be drawn if we consider the masses carried by the colliding and outcoming rings. (The mass is shown in Fig. 6 for $\gamma = 10$ and a qualitative similar picture applies for $\gamma = 7$.) Inspection of Figs. 3 and 6 makes it clear that the incoming and outgoing rings may not carry both the same energy and the same mass. This is because there are no pairs of vortex rings, with velocities of opposite sign, which have the same energy and the same mass. The mass difference should thus have to be carried away by additional excitations created during collision. In conclusion, a bounce-back collision between vortex rings cannot be elastic.

5 Concluding remarks

We have discussed in detail solitary waves in an elongated dilute atomic BEC. These have the form of quasi-1D solitons but they transform to vortex rings in a condensate with sufficiently strong interactions of current experimental interest. We have confined the discussion to axially symmetric solitary waves in a cylindrical trap. Experimental results have been discussed at the end of Sects. 2,3, and 4 which support the argument that axially symmetric solitary waves play a significant role in the condensate dynamics. A more general discussion on solitary waves in a BEC, including non-axisymmetric ones, is given in [47].

The stability of solitary waves is an important issue which will only be discussed here briefly. Solitons are unstable in condensates with strong interactions as has been observed in experiments [15,14]. A stability analysis shows that there is an instability which is due to a non-axisymmetric mode [26]. Subsequently, a non-axisymmetric vortex which may propagate and thus has solitary wave properties has been studied [48,49,35]. It has been called a *solitonic vortex*

and it bifurcates from the soliton at $\gamma = 1.5$. Although the conditions of current experiments should support a solitonic vortex, no observation of this solitary wave has been reported.

Solitary waves can relatively easily be created in condensates with current experimental techniques as demonstrated in experiments [12,13,15,14] (experimental results are reviewed in [50]). Variants of these techniques can be used to create more than one solitary waves and study their interactions [16]. One could thus hope that special properties of solitary waves discussed in this paper could be studied experimentally. In particular, it is an open question whether the impulse defined in (16) has consequencies which could be measured. A closely related issue which was discussed by Kelvin [46] in the context of fluid dynamics is whether a vortex ring colliding on a wall exerts a finite mechanical force. This question has also been discussed theoretically [51–53] and experiments have been performed in superfluid He^4 [54]. The detailed properties of vortex rings presented here is an excellent motivation to study this issue in the context of an atomic BEC.

We return here briefly to the interesting issue of condensates which are confined in non-axisymmetric potentials. In a recent experiment [55] an elongated condensate was created where the confinement frequency in one of the transverse directions was very large. One can write the potential in the form

$$V_{\rm ext}(x,y,z) = \frac{1}{2}\, M\,(\omega_x x^2 + \omega_y y^2 + \omega_z z^2), \tag{22}$$

where we assume that $\omega_x \gg \omega_y, \omega_z$, and $\omega_z < \omega_y$. The condensate geometry is flat and elongated in the z direction. In the simlest case, we suppose that the system is in the ground state in the direction of strong confinement (x), so we write $\Psi(x,y,z) = \xi(x)\psi(y,z)$, where $\xi(x) = 1/(a_x^2\pi)^{1/4}\, e^{-x^2/2a_x^2}$, and $a_x \equiv \sqrt{\hbar/M\omega_x}$ is the oscillator length in the x direction. Using appropriate rationalised units we obtain an equation for the two-dimensional (2D) wavefunction $\psi(y,z)$ which is identical in form to Eq. (7) with the substitution $\gamma \to \gamma_{2d} \equiv \gamma/(\sqrt{2\pi}a_x)$.

One could solve the 2D GP model to obtain solitary wave solutions. The procedure can follow closely the steps described in Sects. 2 and 3 above if we assume that the trap is infinitely-elongated, i.e., $\omega_z = 0$. For $\gamma_{2d} < 1$ we find a quasi-1D soliton with an energy-momentum dispersion qualitatively similar to that shown in Fig. 2. A solitonic vortex is bifurcating from the soliton for $\gamma_{2d} = 0.5$. This is a vortex line along the short (x) direction which is propagating along z [49]. A vortex-antivortex pair which is a steady-state solution propagating with constant velocity exists for $\gamma_{2d} > 1$. The vortex-antivortex pair can be viewed as a projection of a vortex ring in two dimensions. The energy momentum dispersion for solitary waves changes for $\gamma_{2d} > 1$ and it is qualitatively similar to that in Fig. 3a.

The details of vortex-antivortex pairs could be studied in a fashion similar to vortex rings as in Sect. 3. We note that the bifurcation of a soliton to a vortex-antivortex pair in two-dimensions (at $\gamma_{2d} = 1$) occur earlier than the corresponding bifurcation for a vortex ring in 3D (at $\gamma = 4$), a fact which should be attributed to the reduced dimensionality. Furthermore, one can change the value of γ_{2d} simply by changing the strong confinement frequency ω_x. This remark could prove useful in designing a related experiment. Indeed, the parameters of the experiment [55] correspond to values of the nonlinearity parameter γ_{2d} not far from the bifurcation values quoted above.

Acknowledgements

I am grateful to my collaborators Nikos Papanicolaou and Joachim Brand. I acknowledge support from the EPSRC (U.K.) during my work on solitary waves in BEC which is reviewed in the present paper.

References

1. E. A. Cornell and C. E. Wieman, Rev. Mod. Phys. **74**, (2002) 875.
2. W. Ketterle, Rev. Mod. Phys. **74**, (2002) 1131.

3. C. C. Bradley, C. A. Sackett, J. J. Tollett, and R. G.Hulet, Phys. Rev. Lett. **75**, (1995) 1687.
4. V. Bretin, S. Stock, Y. Seurin, and J. Dalibard, Phys. Rev. Lett. **92**, (2004) 050403.
5. L. Lesanovsky and W. von Klitzing, cond-mat/0612213.
6. E. H. Lieb and W. Liniger, Phys. Rev. **130**, (1964) 1605.
7. E. H. Lieb, Phys. Rev. **130**, (1964) 1616.
8. T. Tsuzuki, J. Low Temp. Phys. **4**, (1973) 441.
9. V. E. Zakharov and A. B. Sabat, Sov. Phys. JETP **37**, (1973) 823.
10. P. P. Kulish, S. V. Manakov, and L. D. Faddeev, Theor. Math. Phys. **28**, (1976) 615.
11. M. Ishikawa and H. Takayama, J. Phys. Soc. Japan **49**, (1980) 1242.
12. S. Burger, K. Bongs, S. Dettmer, W. Ertmer, K. Sengstock, A. Sanpera, G.V. Shlyapnikov, and M. Lewenstein, Phys. Rev. Lett. **83**, (1999) 5198.
13. J. Denschlag, J. E. Simsarian, D. L. Feder, Charles W. Clark, L.A. Collins, J. Gubizolles, L. Deng, E.W. Hagley, K. Helmerson, W.P. Reinhardt, S.L. Rolston, B.I. Schneider, and W.D. Phillips, Science **287**, (2000) 97.
14. B.P. Anderson, P.C. Haljan, C.A. Regal, D.L. Feder, L.A. Collins, C.W. Clark, and E.A. Cornell, Phys. Rev. Lett. **86**, (2001) 2926.
15. Z. Dutton, M. Budde, C. Slowe, and L. V. Hau, Science **293**, (2001) 663.
16. N. S. Ginsberg, J. Brand, and L. V. Hau, Phys. Rev. Lett. **94**, (2005) 040403.
17. E. P. Gross, Nuovo Cimento **20**, (1961) 454.
18. E. P. Gross, J. Math. Phys. **4**, (1963) 195.
19. L. P. Pitaevskii, Sov. Phys.-JETP **13**, (1961) 451.
20. S. Komineas and N. Papanicolaou, Phys. Rev. Lett. **89**, (2002) 070402.
21. S. Komineas and N. Papanicolaou, Phys. Rev. A **67**, (2003) 023615.
22. G. Baym and C. J. Pethick, Phys. Rev. Lett. **76**, (1996) 6.
23. V. M. Perez-Garcia, H. Michinel, and H. Herrero, Phys. Rev. A **57**, (1998) 3837.
24. W. P. Reinhardt and C. W. Clark, J. Phys. B **30**, (1997) L785.
25. A. D. Jackson, G. M. Kavoulakis, and C. J. Pethick, Phys. Rev. A **58**, (1998) 2417.
26. A. E. Muryshev, H. B. van Linden van den Heuvell, and G. V. Shlyapnikov, Phys. Rev. A **60**, (1999) R2665.
27. T. Busch and J. R. Anglin, Phys. Rev. Lett. **84**, (2000) 2298.
28. D.L. Feder, M.S. Pindzola, L.A. Collins, B.I. Schneider, and C.W. Clark, Phys. Rev. A **62**, (2000) 053606.
29. L. Salasnich, A. Parola, and L. Reatto, Phys. Rev. A **65**, (2002) 043614.
30. N. G. Parker, N. P. Proukakis, M. Leadbeater, and C. S. Adams, Phys. Rev. Lett. **90**, (2003) 220401.
31. I. V. Barashenkov and E. Y. Panova, Physica D **69**, (1993) 114.
32. G. K. Batchelor, *An Introduction to Fluid Dynamics* (Cambridge University Press, Cambridge, 1967).
33. P. G. Saffman, *Vortex Dynamics* (Cambridge University Press, Cambridge, 1992).
34. C. A. Jones and P. H. Roberts, J. Phys. A: Math. Gen. **15**, (1982) 2599.
35. S. Komineas and N. Papanicolaou, Phys. Rev. A **68**, (2003) 043617.
36. A. D. Jackson and G. M. Kavoulakis, Phys. Rev. Lett. **89**, (2002) 070403.
37. S. Komineas and N. Papanicolaou, Laser Phys. **14**, (2004) 571.
38. R. Donnelly, *Quantized vortices in Helium II* (Cambridge University Press, Cambridge, 1991).
39. L. Carr and C. W. Clark, Phys. Rev. A **74**, (2006) 043613.
40. M. Leadbeater, D.C. Samuels, C.F. Barenghi, and C.S. Adams, Phys. Rev. Lett. **86**, (2001) 1410.
41. C. F. Barenghi, R. J. Donnelly, and W. F. Vinen, *Quantized Vortex Dynamics and Superfluid Turbulence* (Springer-Verlag, Berlin Heidelberg, 2001).
42. M. J. Ablowitz and H. Segur, *Solitons and the inverse scattering transform* (SIAM, 1981).
43. J. Koplik and H. Levine, Phys. Rev. Lett. **76**, (1996) 4745.
44. N. Berloff, J. Phys. A **37**, (2004) 1617.
45. S. Komineas and J. Brand, Phys. Rev. Lett. **95**, (2005) 110401.
46. L. K. S. W. Thomson), Nature (London) **24**, (1881) 47.
47. L. D. Carr and J. Brand, *Multidimensional solitons - Theory*, in preparation (2007).
48. J. Brand and W. P. Reinhardt, J. Phys. B: At. Mol. Opt. Phys. **34**, (2001) L113.
49. J. Brand and W. P. Reinhardt, Phys. Rev. A **65**, (2002) 043612.
50. J. Brand, L. D. Carr, and B. P. Anderson, *Experiments on multidimensional solitons*, in preparation (2007).
51. E. R. Huggins, Phys. Rev. Lett. **29**, (1972) 1067.

52. A. L. Fetter, Phys. Rev. A **6**, (1972) 402.
53. M. C. Cross, Phys. Rev. A **10**, (1974) 1442.
54. G. Gamota and M. Barmatz, Phys. Rev. Lett. **22**, (1969) 874.
55. Z. Hadzibabic *et al.*, Nature **441**, (2006) 1118.